AUTONOMOUS HORIZON-BASED OPTICAL NAVIGATION ON NEAR-PLANAR CISLUNAR LIBRATION POINT ORBITS

Shimane, Yuri; Ho, Koki; Weiss, Avishai

TR2024-139   October 08, 2024

Abstract

We study the use of horizon-based optical navigation on near-planar libration point orbits in cis- lunar space. Particularities that arise from the space- craft's motion being nearly in-plane with the Sun's motion around the Moon are highlighted. The performance is studied through extensive Monte-Carlo simulation using a synthetic image generation pipeline, feeding measurements at various user-defined time intervals to an ex- tended Kalman filter.

4th Space Imaging Workshop 2024

AUTONOMOUS HORIZON-BASED OPTICAL NAVIGATION ON NEAR-PLANAR CISLUNAR LIBRATION POINT ORBITS

Yuri Shimane[1], Koki Ho[1], and Avishai Weiss[2*]; [1]School of Aerospace Engineering (Georgia Institute of Technology), Atlanta, GA 30332), [2]Mitsubishi Electric Research Laboratories (Cambridge, MA 02139). *[weiss@merl.com]

Abstract. *We study the use of horizon-based optical navigation on near-planar libration point orbits in cislunar space. Particularities that arise from the spacecraft's motion being nearly in-plane with the Sun's motion around the Moon are highlighted. The performance is studied through extensive Monte-Carlo simulation using a synthetic image generation pipeline, feeding measurements at various user-defined time intervals to an extended Kalman filter.*

Introduction. With increasing activity in cislunar space, a variety of proposed mission concepts utilize libration point orbits (LPO). Many of these applications rely on autonomous and high-precision navigation to be conducted onboard the spacecraft. As lunar navigational satellite systems (LNSS) do not yet exist, optical navigation (OpNav) enables spacecraft to autonomously collect and process position measurements without reliance on ground-based radiometric updates. OpNav techniques include triangulation,[1,2] horizon-based,[3–5] and terrain-relative methods,[6–8] where the suitability of technique is dependent on the distance from the observation target(s). Horizon-based OpNav makes use of a set of *limb points*, corresponding to points along the lit limb of a celestial object, modeled as an ellipsoid. Within the context of this work, we focus on the scenario where the attitude of the camera is assumed to be known from other sources such as star trackers and inertial measurement units (IMU), and the OpNav algorithm discerns the position vector of the spacecraft with respect to the imaged body. Due to the spherical shape of the Moon and the typical distance from the lunar surface, a sufficient number of limb points can be identified from an image taken by a spacecraft on an LPO provided that the illumination angle is appropriate; thus, horizon-based OpNav is applicable along LPOs.

To date, literature on horizon-based OpNav in cislunar space[9–13] has been centered around concepts such as the Lunar Gateway, which utilizes LPOs with significant out-of-plane components with respect to the Moon's orbital plane around the Earth; from a horizon-based OpNav perspective, the spatial nature of the orbit facilitates the measurement collection, as the Moon has an approximately 90° phase angle while the spacecraft looks at the Moon while flying above the lunar north or south pole. The aforementioned works on OpNav have been motivated by past, present, and future LPO missions, including, e.g., the EQUilibriUm Lunar-Earth point 6U Spacecraft (EQUULEUS)[14] developed by JAXA and the University of Tokyo, the Quenqiao relay satellite developed by CNSA,[15] the Lunar Gateway as part of NASA's Artemis program,[10] and the Lunar Meteoroid Impacts Observer (LUMIO)[9,11] developed by Politecnico di Milano.

In contrast, images taken along a near-planar LPOs are impacted by the phase angle throughout their orbit, and thus present a different type of imaging environment. While to date, no mission has flown a near-planar LPO, orbits such as distant retrograde orbits (DRO) or L1 and L2 Lyapunov orbits have been attracting attention due to their usability as space-based sensor locations for space situational awareness (SSA) and space domain awareness (SDA) applications.[16–19] Previously, Qi and Oguri[12] provided simulation-based results for autonomous navigation on several LPOs including a DRO, leveraging both horizon-based OpNav and GNSS signals, within the circular restricted three-body problem (CR3BP). The authors opted for an approximate model to mimic the behavior of processing an image to obtain limb points, assuming sufficiently many are always available whenever an optical measurement is to be acquired.

In this work, we study the autonomous horizon-based optical navigation problem on near-planar LPOs, specifically looking at a 4:1 resonant DRO and a 1:1 resonant L1 Lyapunov orbit as examples of planar LPOs. Leveraging a synthetic imaging and processing pipeline previously developed by the authors,[13] we make use of a high-fidelity simulation environment, where the performance of an extended Kalman filter (EKF) with full-ephemeris dynamics is investigated. With the incorporation of the synthetic image pipeline and full-ephemeris dynamics, we aim to validate the usability of autonomous horizon-based OpNav that was previously reported in simpler setups.[12]

The remainder of this paper is organized as follows. We first introduce the measurement generation procedure, involving synthetic image generation, image processing, and the Christian-Robinson algorithm[3] to generate a position measurement from the limb points. Next, we discuss near-planar LPOs, focusing on the unique characteristics and challenges associated with conducting OpNav on an LPO that is nearly in-plane with the Sun's motion around the Moon. We then introduce the EKF, the measurement model, and the imaging strategy for autonomous navigation. Insights on horizon-based OpNav performance on the 4:1 resonant DRO and the 1:1 resonant L1 Lyapunov are drawn from Monte-Carlo experiments of synthetic image generation, the Christian-Robinson horizon-based OpNav algorithm, and EKF-based navigation filter. The final section provides concluding remarks.

Horizon-Based Optical Measurements. In this section we introduce the building block for optical navigation: the image generation, processing, and measurement generation algorithm. We begin by providing definitions of the apparent diameter and phase angle that

will be used in subsequent sections for analyzing the Op-Nav problem. We then present the image generation and processing setup that results in pixel coordinates of limb points within the image. Finally, for completeness, we briefly introduce the Christian-Robinson algorithm.

Apparent Diameter and Phase Angle. To evaluate the performance of horizon-based OpNav, we must account for the apparent diameter and the phase angle of the Moon. The apparent diameter, denoted as δ, is given by

$$\delta = 2 \arctan \left(\frac{R_{\text{Moon}}}{\sqrt{r^2 - R_{\text{Moon}}^2}} \right), \tag{1}$$

where R_{Moon} is the radius of the Moon and r is the range from the center of the Moon to the spacecraft.

The phase angle ϕ is given by

$$\phi = \arccos \left(\frac{\boldsymbol{r} \cdot \boldsymbol{r}_{\text{Sun}}}{\|\boldsymbol{r}\|\|\boldsymbol{r}_{\text{Sun}}\|} \right), \tag{2}$$

where $\boldsymbol{r}$ is the position of the spacecraft with respect to the Moon, and $\boldsymbol{r}_{\text{Sun}}$ is the position of the Sun with respect to the Moon. The phase angle also impacts the number of limb points that can be detected based on the relative direction from which the light hits the Moon.

Synthetic Image Generation and Processing. The image is generated using a Blender-based pipeline developed previously by the authors.[13] An example image is shown in Figure 1. Once an image is generated, the pixel coordinates corresponding to the lit limb of the Moon are obtained in three steps:[4] we begin by scanning the image along the illumination direction of the Sun projected onto the image, and create a mask around the pixels where a large jump in intensity is detected. Then, a Canny edge detector is used on the masked image to generate pixel-level accurate lit limb points. Finally, these are refined using the subpixel horizon localization technique using the local Zernike moments of each pixel-level limb point. The illumination scan-based mask is particularly crucial when ϕ is very small, as applying the edge detector directly on the image may result in falsely detecting the terminator as part of the lit limb of the Moon.

Christian-Robinson Algorithm. In this work, we use the Christian-Robinson algorithm[3] to generate a position vector measurement from an image that can then be fed to a dynamic filter. Specifically, we opt for the Singular Value Decomposition (SVD)-variant of the non-iterative algorithm by Christian and Robinson.[3,4] The algorithm generates a position vector measurement and also provides an expression for the analytical covariance.

Consider m detected points on the lit limb of the Moon in pixel coordinates, denoted as $\{u_i, v_i\}_{i=1}^m$. Note that m is dictated by both the apparent diameter and phase angle of the Moon. These are transformed to the image plane vector $\boldsymbol{s}_i \in \mathbb{R}^3$ via

$$\boldsymbol{s}_i = \boldsymbol{\kappa}^{-1} \begin{bmatrix} u_i \\ v_i \\ 1 \end{bmatrix}, \tag{3}$$

Figure 1. Sample synthetic image of the Moon generated with Blender pipeline

where $\boldsymbol{\kappa}$ is the camera calibration matrix.[20] Then, the vector $\boldsymbol{n} \in \mathbb{R}^3$ pointed from the spacecraft camera to the center of the Moon is obtained by solving the least-squares problem

$$\boldsymbol{H}\boldsymbol{n} = \boldsymbol{1}_{m \times 1}, \quad \boldsymbol{H} = \begin{bmatrix} \bar{\boldsymbol{s}}_1^T / \|\bar{\boldsymbol{s}}_1^T\| \\ \vdots \\ \bar{\boldsymbol{s}}_m^T / \|\bar{\boldsymbol{s}}_m^T\| \end{bmatrix}, \tag{4}$$

where $\|\cdot\|$ denotes the Euclidean norm, and $\bar{\boldsymbol{s}}_i$ is given by

$$\bar{\boldsymbol{s}}_i = \boldsymbol{Q}\boldsymbol{T}_{\text{P}}^{\text{C}} \boldsymbol{s}_i, \tag{5}$$

where $\boldsymbol{Q} = \text{diag}(1/a, 1/b, 1/c)$ with a, b, and c corresponding to the Moon's principal axes, and $\boldsymbol{T}_{\text{P}}^{\text{C}} \in \mathbb{R}^{3 \times 3}$ is the transformation matrix from the camera frame to the Moon's principal axes frame. The position vector in the inertial frame, $\boldsymbol{r}$, is obtained from $\boldsymbol{n}$ by

$$\boldsymbol{r} = -\frac{1}{\sqrt{\boldsymbol{n}^T \boldsymbol{n} - 1}} \boldsymbol{T}_{\text{I}}^{\text{P}} \boldsymbol{Q}^{-1} \boldsymbol{n}, \tag{6}$$

where $\boldsymbol{T}_{\text{I}}^{\text{P}} \in \mathbb{R}^{3 \times 3}$ is the transformation matrix from the principal axes frame to the inertial frame, in which the spacecraft dynamics is typically expressed.

The measurement covariance $\boldsymbol{R}$ corresponding to the measurement (6) follows from Christian and Robinson,[3] with appropriate modification due to the use of the SVD, as suggested in Christian,[4] instead of the Cholesky factorization in the original version of the algorithm,[3] and an additional term to model attitude uncertainty. The expression for $\boldsymbol{R}$ is

$$\boldsymbol{R} = \boldsymbol{T}_{\text{I}}^{\text{C}} \left(\boldsymbol{F}\boldsymbol{R}_{\boldsymbol{n}}\boldsymbol{F}^T + \boldsymbol{G}\boldsymbol{R}_\phi \boldsymbol{G}^T \right) \boldsymbol{T}_{\text{C}}^{\text{I}}, \tag{7}$$

where $\boldsymbol{T}_{\text{I}}^{\text{C}} \in \mathbb{R}^{3 \times 3}$ and $\boldsymbol{T}_{\text{C}}^{\text{I}} \in \mathbb{R}^{3 \times 3}$ are, respectively, the transformation matrix from the camera frame to the inertial frame and vice versa. The first term within the brackets in (7) corresponds to variation of the solution

to the least-squares problem (9), while the second term corresponds to variation in ϕ. First, $\boldsymbol{F}$ is given by

$$\boldsymbol{F} = -\left(\boldsymbol{n}^T\boldsymbol{n} - 1\right)^{-1/2}\boldsymbol{T}_{\mathrm{C}}^{\mathrm{P}}\boldsymbol{Q}^{-1}\left(\boldsymbol{I}_{3\times3} - \frac{\boldsymbol{n}\boldsymbol{n}^T}{\boldsymbol{n}^T\boldsymbol{n} - 1}\right), \tag{8}$$

and $\boldsymbol{R_n}$ is the covariance of the least-squares problem (4), given by

$$\begin{aligned}
\boldsymbol{R_n} &= \left[\boldsymbol{H}^T\,\mathrm{diag}(1/\sigma_{y_1}, \ldots, 1/\sigma_{y_m})\boldsymbol{H}\right]^{-1}, \\
\sigma_{y_i} &= \boldsymbol{J}_i\boldsymbol{Q}\boldsymbol{T}_{\mathrm{P}}^{\mathrm{C}}\boldsymbol{R}_s\boldsymbol{T}_{\mathrm{C}}^{\mathrm{P}}\boldsymbol{J}_i^T, \\
\boldsymbol{J}_i &= \frac{1}{\|\bar{\boldsymbol{s}}_i\|}\boldsymbol{n}^T\left(\boldsymbol{I}_{3\times3} - \bar{\boldsymbol{s}}_i'\bar{\boldsymbol{s}}_i'^T\right), \\
\boldsymbol{R}_s &\approx \left(\frac{\sigma_{\mathrm{pix}}}{d_x}\right)^2\begin{bmatrix} 1 & 0 & 0 \\ 0 & 1 & 0 \\ 0 & 0 & 0 \end{bmatrix},
\end{aligned} \tag{9}$$

where σ_{pix} is the standard deviation of observed horizon points on the image, and d_x is the pixel pitch in terms of pixels per radian. In (9), $\boldsymbol{R}_s$ is the covariance of the horizon measurements, for which the approximation from Christian and Robinson[3] has been used. Second, $\boldsymbol{G}$ and $\boldsymbol{R}_\phi$ are given by

$$\begin{aligned}
\boldsymbol{G} &= \boldsymbol{T}_{\mathrm{P}}^{\mathrm{C}}[\boldsymbol{r}_{\mathrm{C}}\times], \\
\boldsymbol{R}_\phi &= \sigma_\phi^2\boldsymbol{I}_3,
\end{aligned} \tag{10}$$

where $[\cdot\times]$ denotes the skew-symmetric following the convention $[\boldsymbol{a}\times]\boldsymbol{b} = \boldsymbol{a} \times \boldsymbol{b}$, and σ_ϕ is the standard deviation the attitude.

Near-Planar Libration Point Orbits. To date, various libration point orbits (LPOs) in cislunar space have been studied for a variety of applications. In practice, LPOs exhibiting an $M{:}N$ resonance, signifying the spacecraft M revolutions within N system period, are typically employed in mission design due to their superior convergence characteristics when constructing the quasi-periodic baseline motion in full-ephemeris dynamics, as well as operation-driven characteristics such as illumination conditions. The system period may be defined with respect to the synodic or sidereal month; in this work, due to the direct implication of the Sun's location on the illumination condition of the Moon, and thereby the performance of OpNav, we employ the synodic period to define resonant LPOs.

Perhaps most well-known and studied today is the 9:2 resonant L2 Near-Rectilinear Halo Orbit (NRHO), which is the planned location for the Lunar Gateway. The EQU-ULEUS mission made use of an approximately 4:1 resonant L2 Halo as its science orbit,[14] while the Queqiao relay satellite was placed in an approximately 2:1 resonant L2 Halo orbit.[15] In the context of OpNav, the Artemis 1 mission was placed on a DRO, where tests on its onboard OpNav capabilities were conducted. Also noteworthy is the Lunar Meteoroid Impacts Observer (LUMIO) mission, which plans to use horizon-based OpNav on a 2:1 resonant L2 Halo orbit for autonomous navigation.[9, 11]
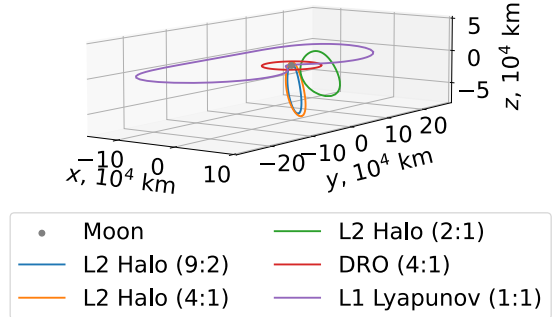

Figure 2. Resonant LPOs studied in the context of horizon-based OpNav in the Circular Restricted Three-Body Problem, shown in the Moon-centered Earth-Moon rotating frame

While there are a number of studies that consider the use of near-planar LPOs such as DROs or Lyapunov orbits, there is little information on the extent to which optical-based autonomous navigation may be performed. In LPOs with significant out-of-plane components, such as the 2:1, 4:1, or 9:2 resonant L2 Halos, the phase angle of the Moon ϕ exhibits a nearly periodic structure about each revolution, where the phase angle near apolune is always approximately $90°$, thus providing reliable measurement opportunities for OpNav. Meanwhile, in near-planar LPOs, the variation of the phase angle is impacted by the fact that the spacecraft's motion is roughly in plane with the Sun's motion with respect to the Moon. In this work, we focus on two planar LPOs: the 4:1 resonant DRO, and the 1:1 resonant L1 Lyapunov orbit. Figure 2 shows the 9:2, 4:1, and 2:1 resonant L2 halo orbits in the CR3BP, along with the two planar LPOs used in this work. The DRO and L1 Lyapunov orbits in the CR3BP in this Figure are used as initial guesses to construct the full-ephemeris quasi-periodic orbits, shown in Figure 3, using a standard multiple shooting approach.[21]

Distant Retrograde Orbit with 4:1 Resonance. The 4:1 resonant DRO constructed in the full-ephemeris dynamics is shown in Figure 3a in the Earth-Moon rotating frame. Figure 4a shows the time history of the apparent diameter and the phase angle across 4 revolutions. The red vertical lines indicate the beginning and end of each revolution, starting at an arbitrary epoch.

We first note that this orbit maintains a roughly constant range from the Moon; thus, the variation in the apparent diameter of the Moon is small as well; this characteristic is favorable for OpNav, as it facilitates the selection of the camera's field of view (FOV). Also noteworthy is the phase angle variation; in the Earth-Moon rotating frame, while the DRO completes 4 revolutions around the Moon clockwise when viewed from the top of the xz-plane, the Sun also completes a single clockwise revolution. As a result, the phase angle experiences 3 full periodic variations over each synodic month.

3

L1 Lyapunov Orbit with 1:1 Resonance. The 1:1 resonant L1 Lyapunov orbit constructed in the full-ephemeris dynamics is shown in Figure 3b in the Earth-Moon rotating frame. Figure 4b shows the time history of the apparent diameter and the phase angle across 2 revolutions, with the red vertical lines indicating again the beginning and end of the two revolutions. The LPO is constructed with an initial phasing along the orbit that achieves near-$0°$ phase angle of the Moon, in line with typical "favorable" observer spacecraft location in SSA and SDA applications.[16–18]

In contrast to the DRO, the L1 Lyapunov has a wide variation in range, which also results in a large variation of the apparent diameter. At perilune, the Moon has a significantly large apparent diameter; however, it is impractical to choose an even larger FOV, as the Moon will appear much smaller during the majority of time. Meanwhile, imaging at perilune is also impractical due to the rapid change in attitude required to successfully align the camera to the Moon; furthermore, while beyond the scope of this work, when the spacecraft flies close to the surface of the Moon, one may opt instead for terrain relative techniques, such as crater-based navigation[6,8] or velocity odometry.[22–24] Thus, omitting to image the entire Moon around the perilune, an FOV of around $5°$ may be employed for the majority of the portion along the LPO. Due to the 1:1 resonance, the phase angle also remains roughly the same except during the perilune pass, leading to favorable imaging conditions for horizon-based OpNav.

Autonomous Navigation. In this Section, we first introduce the translational high-fidelity dynamics model of the spacecraft, followed by a brief overview of the EKF. This is followed by the measurement model used by the EKF, along with the policy used for acquiring an image and producing a measurement for the filter.

Full-Ephemeris Dynamics. The full-ephemeris dynamics considered in this work is the restricted two-body problem centered at the Moon with J2 perturbation of the Moon, solar radiation pressure (SRP), and third-body perturbations from the Earth and the Sun. Let $\boldsymbol{x} \in \mathbb{R}^6$ denote the spacecraft state, composed of the inertial position $\boldsymbol{r} \in \mathbb{R}^3$ and the inertial velocity $\boldsymbol{v} \triangleq \dot{\boldsymbol{r}} \in \mathbb{R}^3$. The dynamics are given by

$$\dot{\boldsymbol{x}} = \begin{bmatrix} \dot{\boldsymbol{r}} \\ \dot{\boldsymbol{v}} \end{bmatrix} = \begin{bmatrix} \boldsymbol{v} \\ -\frac{\mu}{r^3}\boldsymbol{r} + \boldsymbol{a}_{J2} + \boldsymbol{a}_{SRP} + \sum_i \boldsymbol{a}_{N_i} \end{bmatrix}, \quad (11)$$

where μ is the gravitational parameter of the Moon, and the last three terms correspond to the aforementioned perturbation terms. Ephemerides and physical parameters are taken from the SPICE toolkit.[25,26]

Extended Kalman Filter. We consider the use of an extended Kalman filter (EKF) for onboard autonomous navigation by processing the optical measurements. Let $\hat{\boldsymbol{x}}$ denote the state estimate, and $\boldsymbol{P}$ denote the filter covariance; $(\cdot)_{k|k-1}$ denote prior quantities at time k, and $(\cdot)_{k|k}$ denote the posterior quantities at time k. First,

the prediction step consists of integrating the nonlinear dynamics,

$$\hat{\boldsymbol{x}}_{k|k-1} = \int_{t_{k-1}}^{t_k} \boldsymbol{f}(t, \hat{\boldsymbol{x}}_{k-1|k-1})\mathrm{d}t, \quad (12a)$$

$$\boldsymbol{P}_{k|k-1} = \boldsymbol{\Phi}(t_k, t_{k-1})\boldsymbol{P}_{k-1|k-1}\boldsymbol{\Phi}(t_k, t_{k-1})^T + \boldsymbol{Q}_{k|k-1}, \quad (12b)$$

where $\boldsymbol{Q}_{k|k-1}$ is the process noise, modeled as a random process given by

$$\boldsymbol{Q}_{k|k-1} = \sigma_p^2 \begin{bmatrix} \dfrac{\Delta t^3}{3}\boldsymbol{I}_3 & \dfrac{\Delta t^2}{2}\boldsymbol{I}_3 \\ \dfrac{\Delta t^2}{2}\boldsymbol{I}_3 & \Delta t \boldsymbol{I}_3 \end{bmatrix}, \quad (13)$$

with $\Delta t = t_k - t_{k-1}$ and σ_p a tuning parameter. When a measurement is available, we perform the EKF update of the form

$$\boldsymbol{K}_k = \boldsymbol{P}_{k|k-1}\boldsymbol{H}_k^T \left(\boldsymbol{H}_k\boldsymbol{P}_{k|k-1}\boldsymbol{H}_k^T + \boldsymbol{R}_k \right)^{-1}, \quad (14a)$$

$$\hat{\boldsymbol{x}}_{k|k} = \hat{\boldsymbol{x}}_{k|k-1} + \boldsymbol{K}_k \left[\boldsymbol{y}_k - \boldsymbol{h}_k(\hat{\boldsymbol{x}}_{k|k-1}) \right], \quad (14b)$$

$$\boldsymbol{P}_{k|k} = (\boldsymbol{I}_6 - \boldsymbol{K}_k\boldsymbol{H}_k)\boldsymbol{P}_{k|k-1}(\boldsymbol{I}_6 - \boldsymbol{K}_k\boldsymbol{H}_k)^T + \boldsymbol{K}_k\boldsymbol{R}_k\boldsymbol{K}_k^T. \quad (14c)$$

Measurement Model with Horizon-Based Optical Navigation. The Christian-Robinson algorithm yields position vector measurements,

$$\boldsymbol{y} = \boldsymbol{r} + \boldsymbol{\nu}, \quad \boldsymbol{\nu} \sim \mathcal{N}(\boldsymbol{0}, \boldsymbol{R}). \quad (15)$$

The measurement model is thus $\boldsymbol{h}_k(\hat{\boldsymbol{x}}_{k|k-1}) = \boldsymbol{r}_{k|k-1}$, with partials $\boldsymbol{H}_k$ given by

$$\boldsymbol{H}_k = \begin{bmatrix} \boldsymbol{I}_3 & \boldsymbol{0}_{3\times3} \end{bmatrix}. \quad (16)$$

Measurement Collection Strategy. In this work, we assume the boresight of the camera, z_C, is pointed toward the Moon based on the filter's state estimate, with an additional perturbation in its direction to simulate the uncertainty of the attitude. Combining the two effects, z_C is given by

$$z_C = -\boldsymbol{T}(\delta\phi)\frac{\hat{\boldsymbol{r}}}{\|\hat{\boldsymbol{r}}\|}, \quad \delta\phi \sim \mathcal{N}(0, \sigma_\phi), \quad (17)$$

where $\hat{\boldsymbol{r}}$ is the position vector estimate with respect to the Moon, and $\boldsymbol{T}(\delta\phi)$ is the rotation matrix given by the Rodrigues' rotation formula

$$\boldsymbol{T}(\delta\phi) = \cos(\delta\phi)\boldsymbol{I}_3 + \sin(\delta\phi)\boldsymbol{i}^\times + [1 - \cos(\delta\phi)]\boldsymbol{i}\boldsymbol{i}^T. \quad (18)$$

Once the direction of the boresight is decided, the x_C axis is arbitrarily defined as the cross-product between the position and velocity vectors, and the y_C axis completes the triad.

We consider measurement opportunities to occur at a fixed time interval, which we vary between 12, 24, and 48 hours. At a given measurement opportunity, an image is acquired only if (i) the FOV of the OpNav camera exceeds the apparent diameter of the Moon by at least 50%, and (ii) the Sun is outside the FOV.
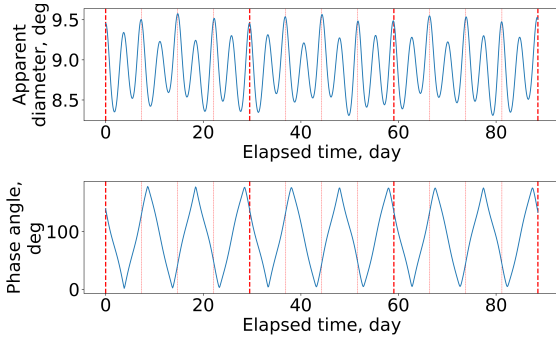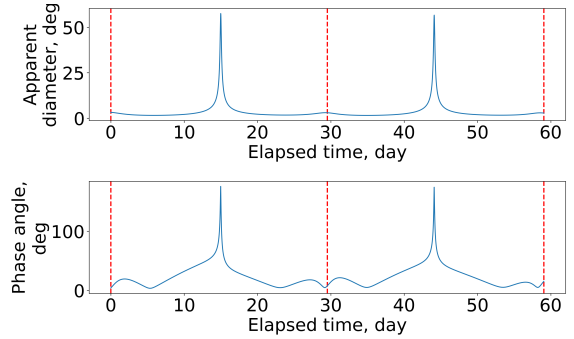
4
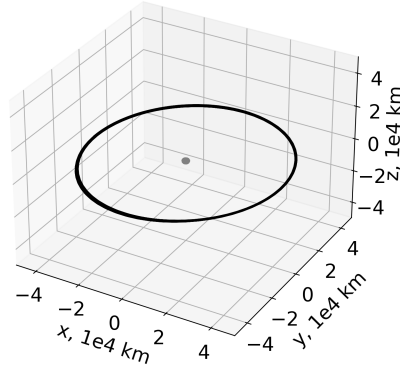
(a) Distant Retrograde Orbit (4:1)
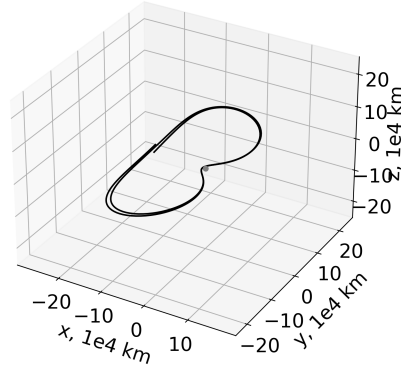
(b) L1 Lyapunov Orbit (1:1)

Figure 3. Planar Libration Point Orbits, computed in the full-ephemeris dynamics, shown in instantaneous Earth-Moon rotating frame centered at the Moon

(a) Distant Retrograde Orbit (4:1)

(b) L1 Lyapunov Orbit (1:1)

Figure 4. Moon's apparent diameter and phase angle history

Results. Navigation with horizon-based optical measurements alone is tested on the 4:1 resonant DRO and the 1:1 resonant L1 Lyapunov orbits. Filter parameters adopted in this work are summarized in Table 1. The camera is assumed to have a square sensor, with the field of views chosen specifically for each LPO based on the phase angle history in Figure 4.

The filter is initialized with a diagonal covariance, given by

$$\boldsymbol{P}_{0|0} = \mathrm{diag}\left(\sigma_{r0}^2, \sigma_{r0}^2, \sigma_{r0}^2, \sigma_{v0}^2, \sigma_{v0}^2, \sigma_{v0}^2\right), \qquad (19)$$

where $\sigma_{r0} = 10\,\mathrm{km}$ is the initial position standard deviation and $\sigma_{v0} = 10\,\mathrm{cm/s}$ is the initial velocity standard deviation. The initial state estimate $\hat{\boldsymbol{x}}_{0|0}$ is sampled from a multivariate normal distribution of $\boldsymbol{P}_{0|0}$.

Uncertainty levels assumed within the simulation are summarized in Table 2. Uncertainty on the dynamics is realized by randomly varying the illuminated area and reflection coefficient pertaining to the SRP term. Each experiment consists of 30 Monte-Carlo runs.

Navigation Performance on Distant Retrograde Orbit. Figure 5 shows EKF results with measurements collected

**Table 1. Filter and simulation parameters**

| Parameter	Value
Canonical length scale LU, km	3000
Canonical time scale TU, sec	2.34671197×10^3
Process noise parameter σ_p	1.8356×10^{-7}
Measurement frequency, hour	12, 24, 48
Pixel standard deviation σ_{pix}, px	0.5
Image size, px×px	1024×1024
Field of view, deg	11.42° (DRO) 5.72° (Lyapunov)

Table 2. Uncertainty parameters

Source	Value
Initial position $3\sigma_{r0}$, km	30
Initial position $3\sigma_{v0}$, cm/sec	30
SRP A/m uncertainty $3\sigma_{A/m}$, %	30
SRP C_r uncertainty $3\sigma_{C_r}$, %	15
Attitude uncertainty $3\sigma_\phi$, arcsec	45
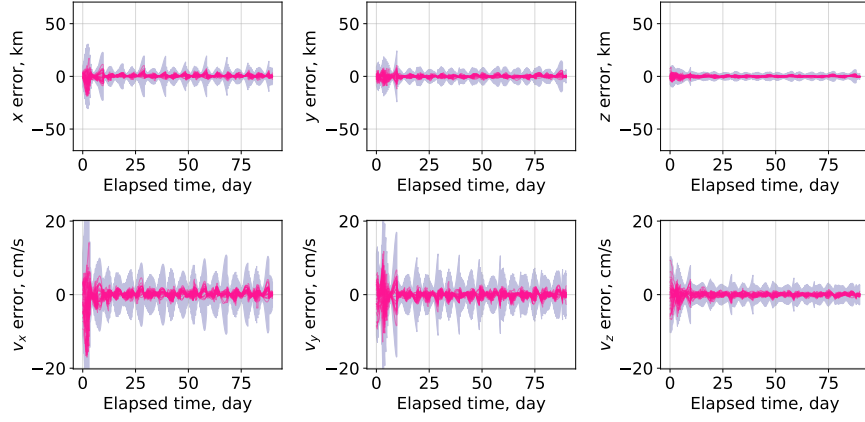
5
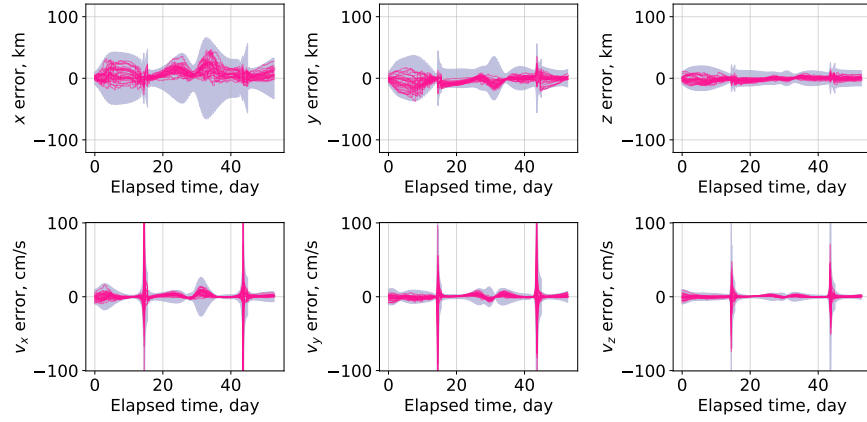
(a) Measurement interval of 12 hours
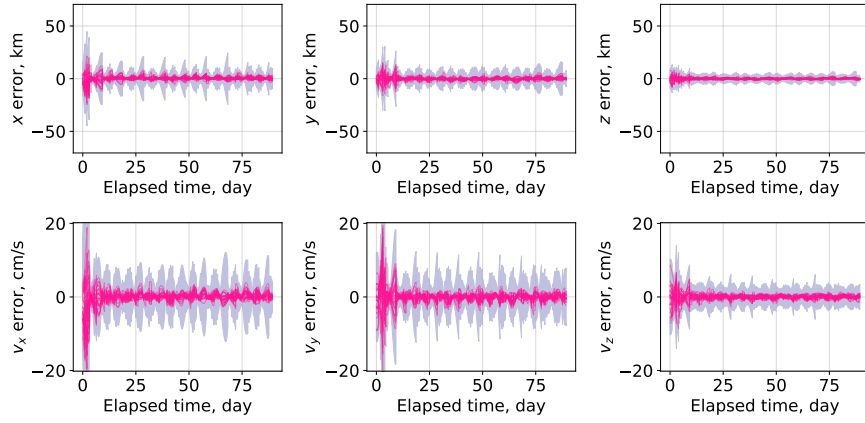
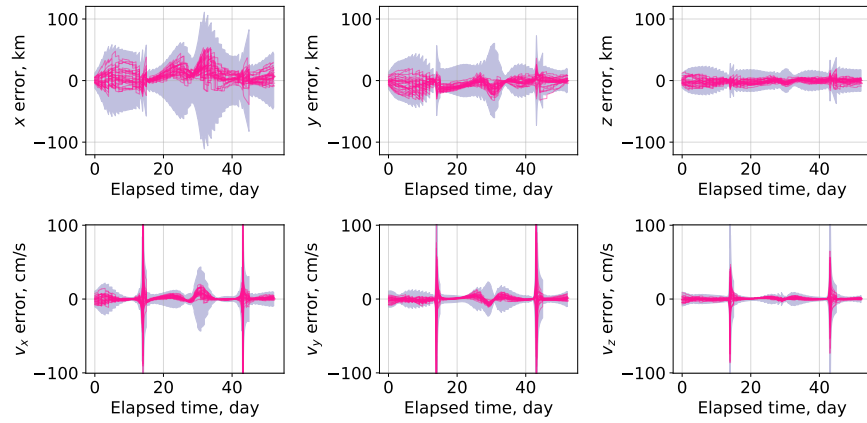*(b) Measurement interval of 24 hours*
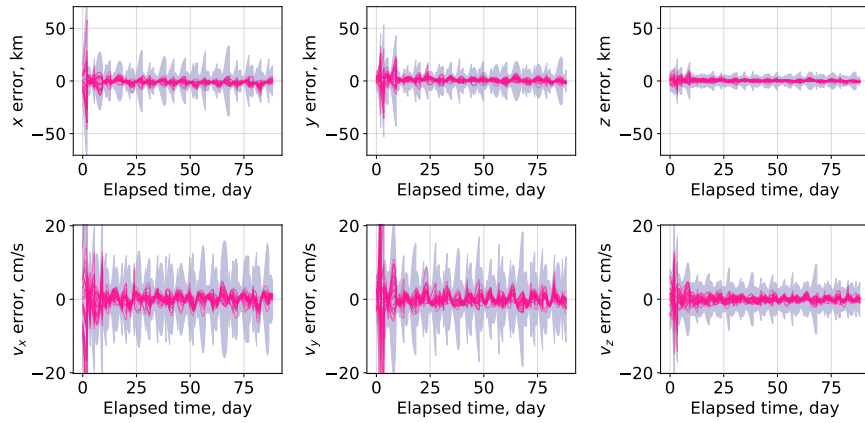
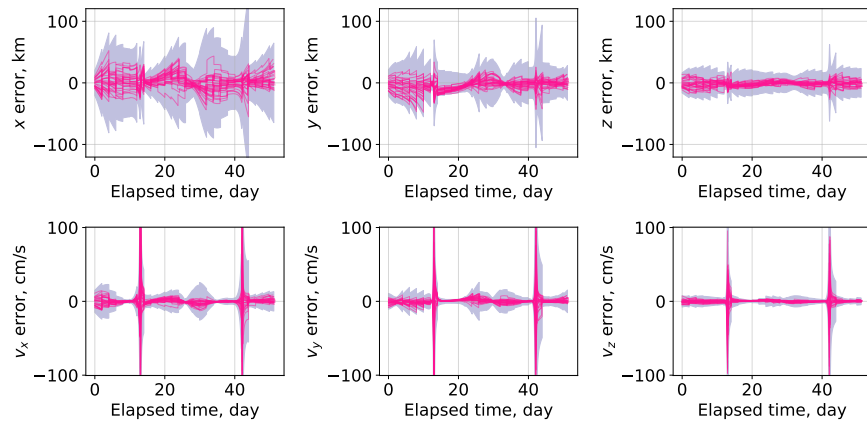*(c) Measurement interval of 48 hours*

Figure 5. Monte-Carlo result of EKF on 4:1 resonant Distant Retrograde Orbit, expressed in Moon-centered J2000 frame

(a) Measurement interval of 12 hours

(b) Measurement interval of 24 hours

(c) Measurement interval of 48 hours

Figure 6. Monte-Carlo result of EKF on 1:1 resonant L1 Lyapunov orbit, expressed in Moon-centered J2000 frame

at 12, 24, and 48-hour intervals, each taking 195, 98, and 49 images over the course of 12 revolutions, respectively. Each state component is in the J2000 inertial frame, in which the equations of motion (11) are resolved. As expected, the filter results in a smaller covariance when the frequency of measurement is higher.

Across all measurement frequencies, we also note the z-component estimation of both position and velocity is better than the estimation of x and y-components position and velocity, respectively. This difference in estimation performance can be attributed to the fundamental degradation in observability along the camera's boresight compared to the x_C and y_C directions. Since the DRO is near-planar, the position vector is primarily composed of x and y components even in the J2000 frame; in contrast, the z component in the J2000 frame is observed through the x_C and y_C directions in the camera frame, which have better observability than z_C.

Navigation Performance on L1 Lyapunov Orbit. Figure 6 shows EKF results with measurements collected at 12, 24, and 48-hour intervals, each taking 107, 54, and 27 images over the course of two revolutions, respectively. Again, increasing the measurement frequency naturally leads to smaller covariance. The perilune pass where no measurement cannot be acquired is found to be under 48 hours; thus, no measurement interruption is seen when the measurement frequency is 48 hours, while the measurement update is briefly interrupted for the 12 and 24-hour cases.

In all cases, a spike in velocity estimation error and covariance, corresponding to perilunes, can be seen. The spike is attributed not only to the large velocity magnitudes during perilune but also to the rapid direction change of the spacecraft; the latter is particularly impacting, as even a slight along-track estimation error can lead to large velocity estimation errors. Similarly to the DRO navigation case, we also observed better filter performance in the L1 Lyapunov orbit in z and v_z components over x and y or v_x and v_y components, respectively; the improved performance is again attributed to the difference in observability along the camera boresight, coupled with the near-planar nature of the LPO.

Conclusions. In this work, we explored the performance of horizon-based optical navigation on near-planar LPOs. The investigation makes use of a synthetic imaging and image processing pipeline, which is then fed to the Christian-Robinson algorithm to generate position vector measurements. The measurements are fed to an EKF, which estimates the translational state of the spacecraft in full-ephemeris dynamics. Monte-Carlo experiments along the 4:1 resonant DRO and 1:1 resonant L1 Lyapunov orbit were conducted for different measurement acquisition frequencies. One noteworthy characteristic of OpNav on near-planar LPO is the impact of the weaker observability along the camera boresight on the navigation filter performance. Overall, this work provides insights into the achievable performance through an autonomous optical navigation scheme in planar LPOs, complementing previous studies conducted on non-planar LPOs.

References.

[1] S. Henry and J. A. Christian, "Absolute Triangulation Algorithms for Space Exploration," *Journal of Guidance, Control, and Dynamics*, vol. 46, pp. 21–46, jan 2023.

[2] S. Henry and J. A. Christian, "Analytical Methods in Triangulation - Based Celestial Localization," *The Journal of the Astronautical Sciences*, pp. 1–26, 2023.

[3] J. A. Christian and S. B. Robinson, "Noniterative Horizon-Based Optical Navigation by Cholesky Factorization," *Journal of Guidance, Control, and Dynamics*, vol. 39, pp. 2757–2765, dec 2016.

[4] J. A. Christian, "Accurate Planetary Limb Localization for Image-Based Spacecraft Navigation," *Journal of Spacecraft and Rockets*, vol. 54, pp. 708–730, apr 2017.

[5] J. A. Christian, "A Tutorial on Horizon-Based Optical Navigation and Attitude Determination with Space Imaging Systems," *IEEE Access*, vol. 9, pp. 19819–19853, 2021.

[6] R. R. Rohrschneider, "Terrain relative navigation using crater identification in surface topography data," in *AIAA Guidance, Navigation, and Control Conference 2011*, 2011.

[7] J. S. McCabe and K. J. DeMars, "Anonymous feature-based terrain relative navigation," *Journal of Guidance, Control, and Dynamics*, vol. 43, no. 3, pp. 410–421, 2020.

[8] J. A. Christian, H. Derksen, and R. Watkins, "Lunar Crater Identification in Digital Images," *Journal of the Astronautical Sciences*, vol. 68, pp. 1056–1144, dec 2021.

[9] V. Franzese, P. Di Lizia, and F. Topputo, "Autonomous optical navigation for the lunar meteoroid impacts observer," *Journal of Guidance, Control, and Dynamics*, vol. 42, no. 7, pp. 1579–1586, 2019.

[10] S. Yun, K. Tuggle, R. Zanetti, and C. D'souza, "Sensor configuration trade study for navigation in near rectilinear halo orbits," in *Advances in the Astronautical Sciences*, vol. 171, pp. 2799–2812, Univelt Inc., 2020.

[11] C. X. Wu, P. Machuca, L. Felicetti, and J. P. Sanchez, "Autonomous Optical Navigation for Small Spacecraft in Cislunar Space," in *73rd International Astronautical Congress (IAC)*, no. September, pp. 18–22, 2022.

[12] D. C. Qi and K. Oguri, "Analysis of Autonomous Orbit Determination in Various Near-Moon Periodic Orbits," *Journal of the Astronautical Sciences*, vol. 70, no. 6, pp. 1–30, 2023.

[13] Y. Shimane, P. Miraldo, K. Berntorp, M. Greiff, P. Elango, and A. Weiss, "High-Fidelity Simulation of Horizon-Based Optical Navigation with Open-Source Software," in *International Astronautical Congress (IAC)*, (Baku, Azerbaijan), 2023.

[14] K. Oguri, K. Oshima, S. Campagnola, K. Kakihara, N. Ozaki, N. Baresi, Y. Kawakatsu, and R. Funase, "EQUULEUS Trajectory Design," *Journal of the Astronautical Sciences*, 2020.

[15] S. Qin, Y. Huang, P. Li, Q. Shan, M. Fan, X. Hu, and G. Wang, "Orbit and tracking data evaluation of Chang'E-4 relay satellite," *Advances in Space Research*, vol. 64, no. 4, pp. 836–846, 2019.

[16] J. K. Vendl and M. J. Holzinger, "Cislunar Periodic Orbit Analysis for Persistent Space Object Detection Capability," *Journal of Spacecraft and Rockets*, vol. 58, no. 4, pp. 1174–1185, 2021.

[17] L. Visonneau, Y. Shimane, and K. Ho, "Optimizing Multi-spacecraft Cislunar Space Domain Awareness Systems via Hidden-Genes Genetic Algorithm," *The Journal of the Astronautical Sciences*, vol. 70, p. 22, jul 2023.

[18] Y. Shimane, K. Tomita, and K. Ho, "Cislunar constellation design for space situational awareness with time-expanded facility location problem," 2024.

[19] M. Patel, Y. Shimane, H. W. Lee, and K. Ho, "Cislunar Satellite Constellation Design via Integer Linear Programming," *The Journal of the Astronautical Sciences*, vol. 71, p. 26, may 2024.

[20] R. Hartley and A. Zisserman, *Multiple View Geometry in Computer Vision*. New York, NY, USA: Cambridge University Press, 2 ed., 2003.

[21] J. Williams, D. E. Lee, R. J. Whitley, K. A. Bokelmann, D. C. Davis, and C. F. Berry, "Targeting cislunar near rectilinear halo orbits for human space exploration," in *AAS/AIAA Space Flight Mechanics Meeting*, 2017.

[22] D. Zuehlke, D. Posada, M. Tiwari, and T. Henderson, "Autonomous Satellite Detection and Tracking using Optical Flow," pp. 1–11, apr 2022.

[23] C. De Vries, J. Christian, M. Hansen, and T. Crain, "Lidar Odometry for Lunar Terrain Relative Navigation," in *AAS/AIAA Astrodynamics Specialist Conference*, 2022.

[24] G. Molina, M. Hansen, J. Getchius, R. Christensen, J. A. Christian, S. Stewart, and T. Crain, "Visual Odometry for Prevision Lunar Landing," in *AAS/AIAA Astrodynamics Specialist Conference*, 2022.

[25] C. Acton, "Ancillary data services of NASA's navigation and Ancillary Information Facility," *Planetary and Space Science*, vol. 44, no. 1 SPEC. ISS., pp. 65–70, 1996.

[26] C. Acton, N. Bachman, B. Semenov, and E. Wright, "A look towards the future in the handling of space science mission geometry," *Planetary and Space Science*, vol. 150, no. January 2017, pp. 9–12, 2018.